Advanced Electronic Materials

ADVANCED ELECTRONIC MATERIALS Open Access

www.advelectronicmat.de

RESEARCH ARTICLE OPEN ACCESS

Side-Chain Branching Dictates the σ–S Coupling in Conjugated Polymer Thermoelectrics

Yingyao Zhang[1,2,3] | So-Huei Kang[4,5,6] | Po Chen[1,2,3] | Huadeng Xie[1,2,3] | Qinfang Zhang[1,2,3] | Seoyoung Kim[4] | Donghoo Won[4] | Zilong Zhang[1,2,3] | Chi Li[1,2,3] | Liang Liu[7] | Qi Zhu[7] | Feiyan Wu[7] | Lie Chen[7] | Reza Keshavarzia[8] | Changduk Yang[4,5,9] | Peng Gao[1,2,3]

[1]State Key Laboratory of Structural Chemistry, Fujian Institute of Research on the Structure of Matter, Chinese Academy of Sciences, Fuzhou, Fujian, China | [2]Xiamen Key Laboratory of Rare Earth Photoelectric Functional Materials, Xiamen Institute of Rare Earth Materials, Chinese Academy of Sciences, Xiamen, China | [3]Fujian College, University of Chinese Academy of Sciences, Fuzhou, China | [4]Department of Energy Engineering, School of Energy and Chemical Engineering, Ulsan National Institute of Science and Technology (UNIST), 50 UNIST-gil, Ulju-gun, Ulsan, Republic of Korea | [5]UNIST InnoCORE AI-Space Solar Initiative, Ulsan National Institute of Science and Technology (UNIST), Ulsan, Republic of Korea | [6]Department of Chemistry, McGill University, Quebec, Canada | [7]College of Chemistry, Nanchang University, Nanchang, China | [8]Department of Chemistry, University of Isfahan, Isfahan, Iran | [9]Graduate School of Carbon Neutrality, Ulsan National Institute of Science and Technology (UNIST), 50 UNIST-gil, Ulju-gun, Ulsan, South Korea

Correspondence: Reza Keshavarzia (R.Keshavarzi@chem.ui.ac.ir) | Changduk Yang (yang@unist.ac.kr) | Peng Gao (peng.gao@fjirsm.ac.cn)

Received: 5 January 2026 | **Accepted:** 10 March 2026

Keywords: couple | density of state distribution | organic thermoelectric materials | side-chain engineering

ABSTRACT

Understanding the intrinsic coupling between electrical conductivity (σ) and the Seebeck coefficient (S) remains a central challenge in organic thermoelectrics, where energetic disorder and charge transport are highly sensitive to molecular design. Here, we show that precise control over the *side-chain branching position* provides an effective structural lever to tune the σ–S relationship in conjugated polymers. Two DPP–selenophene copolymers with identical backbones but branched at distinct positions exhibit markedly different molecular packing, charge-carrier delocalization, and density-of-states (DOS) widths. Polymers with more distant branching points form tighter π–π stacks, yielding enhanced carrier mobility and a narrower DOS that collectively boost σ to 129.3 S cm^{-1}. In contrast, closer branching induces greater energetic disorder and broader DOS distributions, resulting in a substantially higher S of 160 μV K^{-1}. Despite their contrasting transport characteristics, both polymers deliver similar peak power factors owing to complementary changes in σ and S. These results identify side-chain branching as a previously underappreciated design parameter that mechanistically governs the coupling between conductivity and Seebeck coefficient in organic thermoelectric materials.

1 | Introduction

Organic thermoelectric materials (OTEMs) have emerged as promising candidates for lightweight, flexible, and low-thermal-conductivity energy harvesters capable of converting ubiquitous temperature gradients into electrical power [1–5]. Among them, donor–acceptor (D–A) copolymers have attracted particular attention due to their tunable electronic structures and favorable doping characteristics [6–8]. In p-type systems, donor units facilitate charge transfer during chemical doping, while acceptor units introduce energetic disorder along the π-backbone, often enhancing the Seebeck coefficient (S) [9].

Yingyao Zhang, So-Huei Kang, and Po Chen contribute equally to this work.

Diketopyrrolopyrrole (DPP)-based copolymers—including PDPP-4T-EDOT [10], FBDPPV [11], PSeDPPBT [12, 13], and A-DCV-DPPTT [14] —represent state-of-the-art OTEMs, underscoring the important role of backbone engineering [15].

Like their inorganic counterparts, the performance of OTEMs is usually parameterized by the dimensionless figure of merit, $zT = S^2\sigma T/\kappa$, where S, σ, T, and κ represent Seebeck coefficient, electrical conductivity, absolute temperature, and total thermal conductivity, respectively. Due to the inherent low κ of organic materials, the evaluation of OTEM's properties also encompasses the power factor (PF), as determined by $PF = S^2\sigma$. Obviously, OTEMs with simultaneous high σ and S could provide the best PF. However, a critical hurdle in developing efficient OTEMs could be seen from the inverse relationship between σ and S as defined by $S = \frac{1}{\sigma}(\frac{k_B}{e})\int_{-\infty}^{\infty}\sigma_E(E,T)(\frac{E-E_F}{k_BT})(-\frac{df}{dE})dE$, where k_B is Boltzmann's constant, e is the fundamental charge, $\sigma_E(E,T)$ is the transport function, E is electron energy, E_F is the Fermi energy level, and f is the Fermi-Dirac distribution function [16, 17]. This means that the monotonic increase in electrical conductivity (σ) does not directly lead to a decrease in the Seebeck coefficient (S). Instead, the decrease in S arises from the relative weight of conductivity at different energies, as governed by the energy-weighted average conductivity. The reduction in the Seebeck coefficient is primarily due to the narrowing of the transport window around the Fermi energy (E_F), making carriers near EF dominant in transport. Thus, the inverse relationship between σ and S should be attributed to the impact of energy-weighted conductivity on the Seebeck coefficient, rather than the absolute magnitude of σ. Consequently, this effect results in an extremum in the product (PF) of σ and S [18–20]. While achieving the highest PF value necessitates a delicate balance between S and σ, numerous strategies—including dopant selection [21, 22], doping level optimization [23], backbone planarity control [24], and heteroatom incorporation [25]—have been employed to mitigate this σ–S trade-off [26]. However, most studies have focused on backbone or dopant design, whereas the influence of side-chain architecture, which strongly affects molecular packing, energetic disorder, and dopant incorporation, remains comparatively underexplored.

Here, we uncover a previously unrecognized mechanism by which side-chain branching governs the intrinsic coupling between σ and S. Using two D–A conjugated polymers—PDPPSe-2 and PDPPSe-5—that share an identical backbone but differ only in the distance between the branching point and the backbone, we reveal how subtle variations in side-chain topology can systematically modulate microstructure, charge-carrier delocalization, and density-of-states (DOS) width. (Table S1) PDPPSe-5, with a more distant branching point, exhibits tighter π–π stacking, higher mobility, and enhanced carrier delocalization, resulting in superior conductivity upon $FeCl_3$ doping [27–29]. Conversely, the closer branching point in PDPPSe-2 induces greater energetic disorder and broader DOS distributions, yielding a significantly higher Seebeck coefficient. Despite their divergent transport behaviors, both polymers achieve comparable maximum power factors due to compensating changes in σ and S. These results establish side-chain branching as a powerful, previously underappreciated molecular design parameter that directly tunes the σ–S relationship in conjugated polymers, offering new insight into the structure–property origins of thermoelectric performance.

2 | Result and Discussion

Figure 1a illustrates the chemical structures of the D-A copolymers PDPPSe-2 and PDPPSe-5, of which the backbones were composed of selenophene (Se) as a donor and DPP structure as an acceptor. Notably, the two polymers differ by a subtle change in the branching sites on their side chains: forking at C2 for PDPPSe-2 and at C5 for PDPPSe-5, respectively. It is important to note that matching the energy levels between OSCs and dopants is crucial for the doping process [27, 30]. Specifically, the HOMO level of OSCs should be shallower than the LUMO level of dopants, and a larger level offset aids in facilitating the charge transfer process. To determine the suitability of PDPPSe-2 and PDPPSe-5 for doping, cyclic voltammetry (CV) measurements were performed (Figure S2). The results show that different side chains yield distinct HOMO levels, with -5.27 eV for PDPPSe-2 and −5.26 eV for PDPPSe-5. Consequently, $FeCl_3$, which possesses a deeper LUMO level (−5.85 eV) [31], was selected for an effective chemical doping process. A schematic diagram illustrating the electron transfer process is depicted in Figure 1b.

Different molecular structures often result in changes in optical spectra. UV–vis-NIR spectroscopy reveals that the π-π* peak of PDPPSe-5 shifts toward a higher wavelength compared to PDPPSe-2 (Table S2), indicating that PDPPSe-5 possesses stronger intramolecular conjugation ability. Notably, after doping with $FeCl_3$ solution, interesting phenomena occur. Both polymers exhibit a reduced peak at 800–900 nm and a new polaron absorption band in the 1200~1300 nm range. (Figure 1c,d) This confirms the occurrence of the doping process and the formation of polaronic species [32, 33]. Interestingly, a new peak appears in the range below 500 nm and becomes stronger under higher doping levels, which could be caused by the incompletely reacted neutral $FeCl_3$ dopants. Since we primarily focus on the impact of different polymer structures on doping efficiency and thermoelectric properties at the same doping level, conditions with higher dopant concentrations are not discussed.

Subsequently, a semi-quantitative analysis of the doping level was performed using the ratio of the π-π* peak to the polaron absorptions ($I_{Polaron}/I_{\pi\text{-}\pi^*}$) (Figure 1e; Table S2) [34, 35]. PDPPSe-5 demonstrates a higher doping level at low doping concentrations. This is likely due to steric reasons; the longer side chains provide more attachment sites for dopant molecules, thereby facilitating the doping process. Moreover, the density functional theory (DFT) calculations (Figures S3 and S4) illustrate that the energy required for the dopant to react with PDPPSe-5 is significantly lower than that of PDPPSe-2. However, with a further increase in doping concentration, its doping efficiency decreases to a level lower than that of PDPPSe-2. This is attributed to the destruction of the internal film structure caused by the high doping concentration, as elucidated by subsequent GIWAXS characterization.

Intriguingly, as the doping concentration increases, the π-π* peak experiences a blue shift while the polaron absorptions undergo a red shift, as exhibited in Figure 1f and Table S2. The

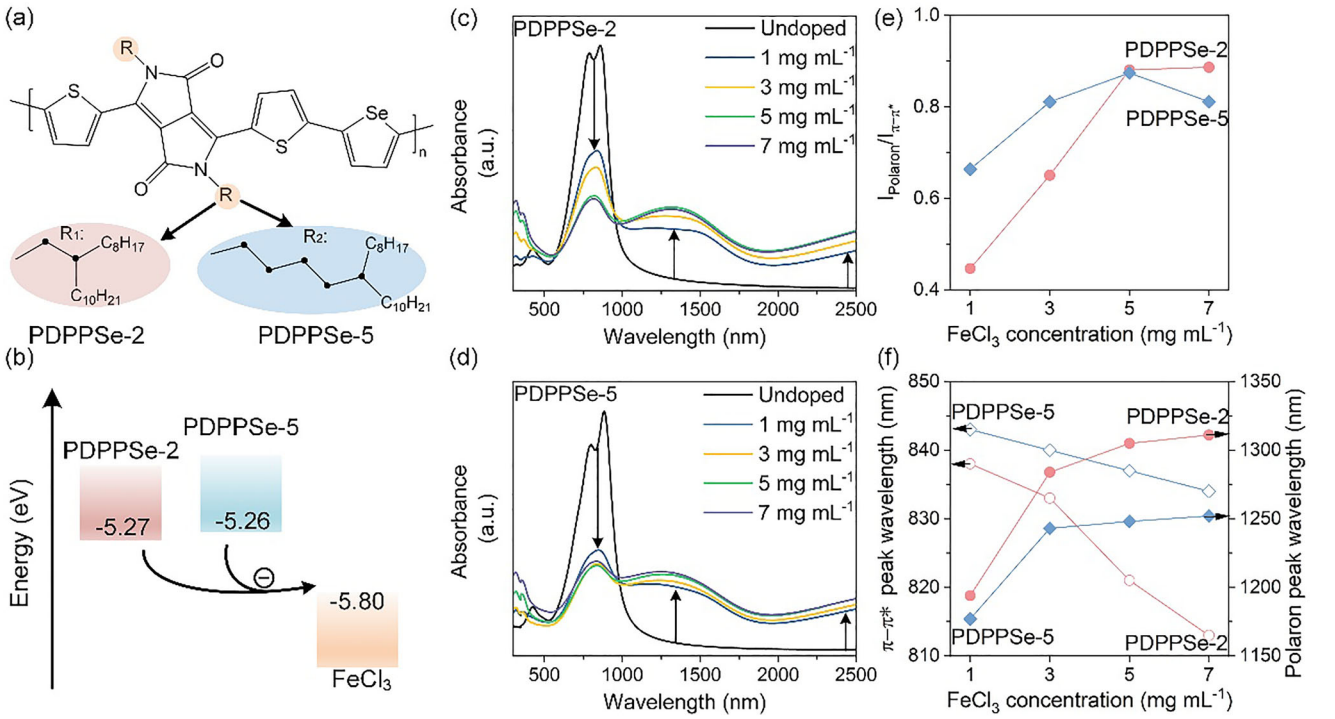

FIGURE 1 | (a) Chemical structures of PDPPSe-2 and PDPPSe-5. (b) a schematic illustration describing the electron transfer process between polymers and $FeCl_3$. UV–vis-NIR absorption spectra are presented for (c) PDPPSe-2 and (d) PDPPSe-5 films at different dopant concentrations. The corresponding (e) polaron concentrations and (f) wavelength variations are also displayed. The pink circles represent PDPPSe-2, the blue prisms represent PDPPSe-5, and solid and hollow dots represent the variation of π-π* peak and polaron absorptions, respectively.

former indicates that the doping process reduces intramolecular conjugation by incorporating dopant molecules. Meanwhile, the latter confirms that the Coulomb interaction between the polaron and the dopant counterion gradually intensifies as the doping progresses. Moreover, the wavelength of the π-π* peak in PDPPSe-5 consistently surpasses that of PDPPSe-2 across all doping levels, indicating stronger conjugation ability in doped PDPPSe-5. However, regarding the polaron absorptions, the two films exhibit a trend opposite to that of the π-π* peak. This divergence arises from the shorter side chain of PDPPSe-2, which intensifies Coulomb interactions between the dopant antiparticle and the polymer backbone.

GIWAXS was used to characterize the microstructure and molecular packing of polymer films at various dopant concentrations. Notably, the diffraction peaks of PDPPSe-5 display higher-order peaks in comparison to PDPPSe-2 (Figure 2a,b; Figures S5–S8), suggesting superior crystallization properties of PDPPSe-5 polymer films. Additionally, both polymer films exhibit a predominant edge-on orientation, and the weaker in-plane peak for PDPPSe-2 is due to its generally weaker diffraction.

Furthermore, 1D GIWAXS analysis was employed to determine the π-π stacking distance (d_π), lamellar structure (d_l), and corresponding crystalline coherence lengths (CCL) (Figure 2c,d). By altering the alkyl spacer from a methyl (PDPPSe-2) to a butyl unit (PDPPSe-5), the d_π is reduced from 3.83 to 3.70 Å. This reduction facilitates better charge transport, likely due to the alleviation of steric side effects caused by the alkyl chains on the conjugated backbone. Accordingly, the hole mobility of PDPPSe-5-based films reaches a higher value of 7.68 $cm^2\ V^{-1}\ s^{-1}$ compared to 1.54 $cm^2\ V^{-1}\ s^{-1}$ for PDPPSe-2, as observed through organic field-effect transistor characterization (Figure S9).

Notable changes are observed in the GIWAXS spectra after the doping process. Initially, the calculated d_π for both polymers decreases to a minimum as the doping concentration increases. However, a further increase in the doping concentration disrupts molecular packing, reversing this trend. Remarkably, the concentration of 5 mg mL^{-1} represents the turning point for PDPPSe-5, while for PDPPSe-2, it occurs at 9 mg mL^{-1} (left panels in Figure 2c,d). The destruction of molecular packing underlies the alteration in the doping level (Figure 1e).

Notably, a longer side chain results in a larger d_l value of 27.44 Å for undoped PDPPSe-5, compared to 22.28 Å for PDPPSe-2. (Table S3) Although the shorter d_l may be beneficial for charge transport, the number of layers (N_l) estimated from CCL/dl provides a more accurate assessment of the combined effects of layer distance and crystallite size. The N_l of PDPPSe-2 and PDPPSe-5 was estimated to be 5.0 and 7.4 layers, respectively. This may account for the relatively lower mobilities observed in PDPPSe-2. Additionally, the doping process increases the d_l for both polymers, primarily due to the insertion of dopant molecules. Furthermore, PDPPSe-5 outperforms PDPPSe-2 in crystallinity, resulting in higher CCL. Consequently, PDDPSe-5 exhibits diffraction peaks up to the fifth order, whereas PDPPSe-2 exhibits only fourth-order peaks.

The doping process can be divided into two stages: charge transfer and the release of free carriers, the latter of which

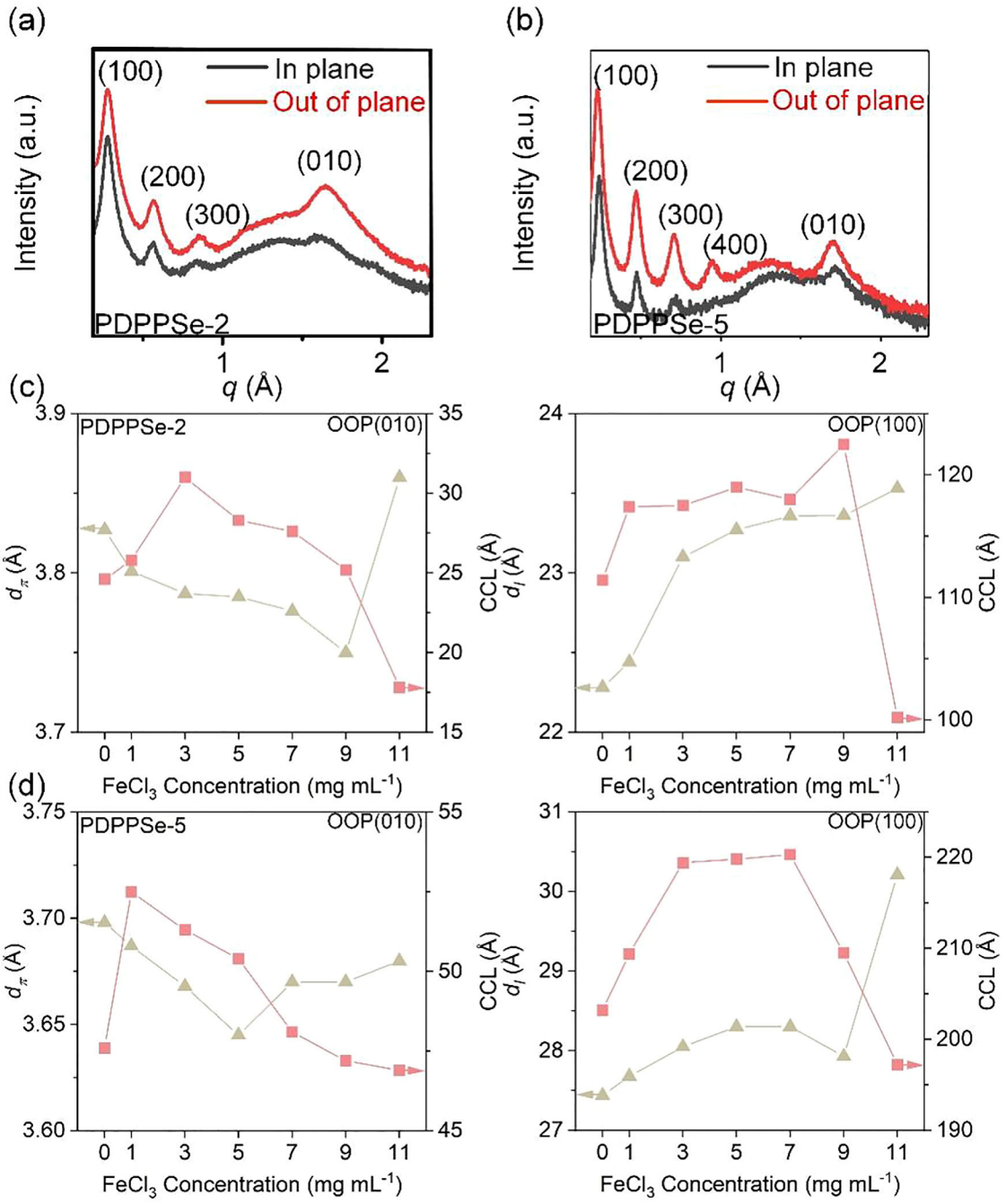

FIGURE 2 | GIWAXS patterns of (a) PDPPSe-2 and (b) PDPPSe-5 thin films. The *d*-spacing of π-π stacking diffraction (d_π) and lamellar structure (d_l), along with the respective crystalline coherence length (CCL) at different out-of-plane (OOP) directions: (c) for PDPPSe-2 and (d) for PDPPSe-5 at various $FeCl_3$ concentrations. The green circles and pink triangles depict *d*-spacing and corresponding CCL, respectively.

significantly affects charge transport [9]. Significant Raman signals from C═C stretches in the DPP and Se units were observed in the Raman characterization of the polymers. As shown in Figure 3a,b, PDPPSe-5 exhibits a more pronounced downshift in Raman frequency, indicating a higher degree of charge-carrier delocalization, which is expected to facilitate charge transport [36]. The distant side-chain branching could weaken Coulombic interactions between $FeCl_3$ anions and polarons in the polymer backbone, thereby enhancing charge transfer.

In the electrical conductivity results, both doped PDPPSe-2 and PDPPSe-5 achieved a high conductivity (σ). The maximum conductivity of doped PDPPSe-2 reached 99.55 S cm^{-1}, while a remarkable maximum conductivity of 129.30 S cm^{-1} was attained for doped PDPPSe-5 (Figure 4a). This highlights the significance of both charge-transport ability and the degree of charge-carrier delocalization in achieving higher conductivity.

In addition, both doped polymers exhibit a positive *S* value, indicating their p-type nature. (Figure S11) As expected, the

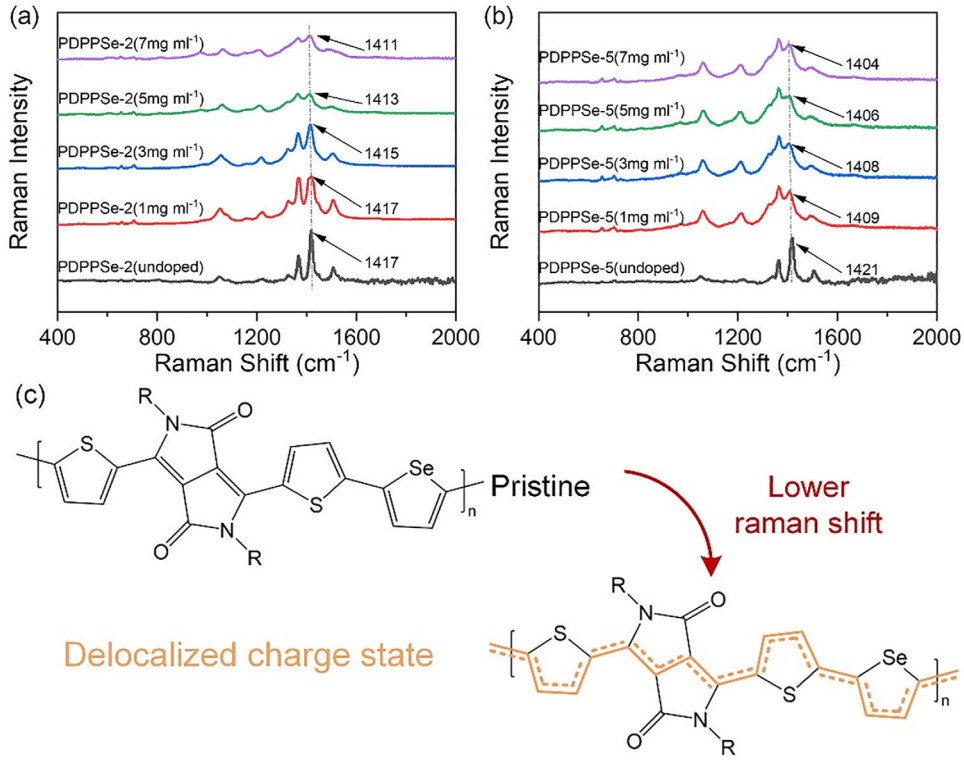

FIGURE 3 | Raman spectra of (a) PDPPSe-2 and (b) PDPPSe-5 before and after doping. (c) Schematic representation of a delocalized charge state after doping.

Seebeck coefficient (S) decreases with increasing doping levels. This reduction arises from the enhanced density of conducting states near the Fermi level, caused by the higher charge-carrier concentration introduced by doping, as further confirmed by electrochemical characterization.

To date, numerous empirical laws have been used to elucidate the intrinsic coupling between σ and S, revealing a negative correlation between the two [16, 17, 37]. Moreover, S can be fitted to an empirical power law: [37]

$$S = \frac{k_B(\sigma/\sigma_0)^{-\frac{1}{4}}}{e}$$

where k_B is the Boltzmann constant, σ_0 is an unknown conductivity constant independent of carrier concentration in the covered range, and e is the electron charge constant. Additionally, PDPPSe-2 exhibits a higher S value than PDPPSe-5, and the reason for this will be discussed below. Furthermore, a linear relationship of $S \propto \sigma^{-1/4}$ is observed between σ and S (Figure 4b).

Figure 4d is a schematic illustration, adapted from the literature, that conceptually summarizes the role of density-of-states (DOS) engineering in conjugated polymers [38]. This schematic highlights the general trade-off among electrical conductivity, carrier mobility, and Seebeck coefficient as a function of DOS width. In doped conjugated polymers, a broader DOS is typically associated with enhanced dopant miscibility and higher carrier concentration, which favors high electrical conductivity, whereas a narrower DOS reduces energetic barriers for hopping transport and thus promotes higher carrier mobility. As a result, optimal thermoelectric performance requires a moderate DOS width that balances carrier concentration and energetic disorder.

Guided by this conceptual framework, we further investigated the microscopic origin of the observed σ–S trends by experimentally probing the DOS distributions of PDPPSe-2 and PDPPSe-5 films using electrochemical measurements [38, 39]. As shown in Figure 4e,f, PDPPSe-2 exhibits a broader density-of-states (DOS) distribution compared to PDPPSe-5, indicating a higher degree of energetic disorder. In doped organic semiconductors operating in the hopping regime, a broader DOS increases the relative contribution of higher-energy tail states to charge transport. This shifts the average transport energy further away from the Fermi level, thereby increasing the Seebeck coefficient. Consequently, the higher Seebeck coefficient observed for PDPPSe-2 can be directly attributed to its broader DOS and enhanced energetic disorder [40, 41]. Obviously, the value of S decreases with increasing doping levels. This is primarily due to the rise in conducting states near the Fermi energy, which results from the increased charge carrier concentration induced by doping, as confirmed by subsequent electrochemical characterization.

Although the DOS broadens with increasing doping concentration (Figure S10), the experimentally observed decrease in the Seebeck coefficient at higher doping levels does not originate from DOS broadening alone. Instead, increased doping shifts the Fermi level deeper into the DOS and narrows the effective transport window around E_F, thereby dominating charge transport by states closer to the Fermi energy. This reduced energy asymmetry in transport results in a lower Seebeck coefficient, despite concurrent DOS broadening [42, 43].

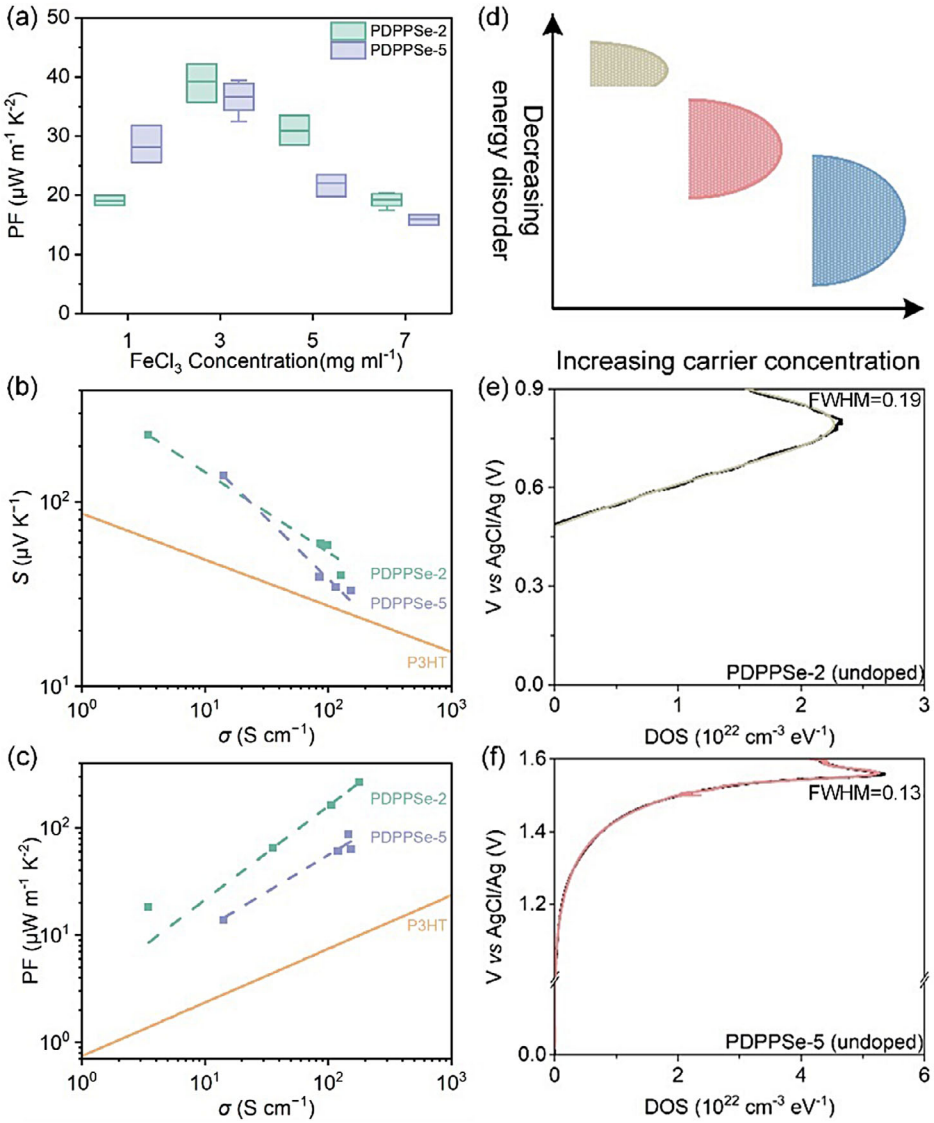

FIGURE 4 | (a) Power factor for PDPPSe-2 and PDPPSe-5 films doped with different $FeCl_3$ concentrations. (b) Seebeck coefficient and (c) power factor as a function of electrical conductivity. The green solid lines showing the P3HT data are fitted based on the literature [37]. The cyan and blue-violet dashed lines are fitted to the experimental data of PDPPSe-2 and PDPPSe-5, respectively. (d) Schematic diagram of DOS distributions as a function of carrier concentration and energy disorder [38]. DOS distributions and Gaussian-fitted curves of undoped (e) PDPPSe-2 and (f) PDPPSe-5. The green and red lines are Gaussian-fitted to the experimental data.

We note that fitting the DOS distributions inevitably introduces some uncertainty, as the Gaussian tails extend beyond the measured potential window. Nevertheless, within the experimental range, the onset position remains essentially constant, while the distribution width increases with doping. This trend indicates that disorder-induced broadening, rather than a rigid energy shift, governs the DOS evolution and accounts for the concurrent reduction in the Seebeck coefficient (S) at higher doping levels.

Unlike metals, where the Seebeck coefficient is primarily determined by the slope of the DOS at the Fermi level, charge transport in doped organic semiconductors involves a broad energy window. As a result, the Seebeck coefficient is governed by the energy-weighted average of the conductivity over the DOS, rather than by the local DOS slope at E_F [44]. Broadening the doping range lowers this slope, weakening the energy-asymmetric transport that underpins S and thereby reconciling the measured decrease in the Seebeck coefficient with the DOS evolution.

Finally, PF was calculated from σ and S. For PDPPSe-2, the maximum PF is 42.19 μW m^{-1} K^{-2}. Despite doped PDPPSe-5 having a higher σ, its low S yields a maximum PF of 39.40 μW m^{-1} K^{-2}, similar to that of PDPPSe-2 (Figure S11). This suggests that the molecular structure can selectively enhance σ and S. Additionally, the empirical relationship between σ and PF (PF $\propto \sigma^{1/2}$) is corroborated in Figure 4c.

Furthermore, we investigate the aggregated features of the OSC films, which may influence their performance [45, 46], using atomic force microscopy (AFM). Thanks to the enhanced

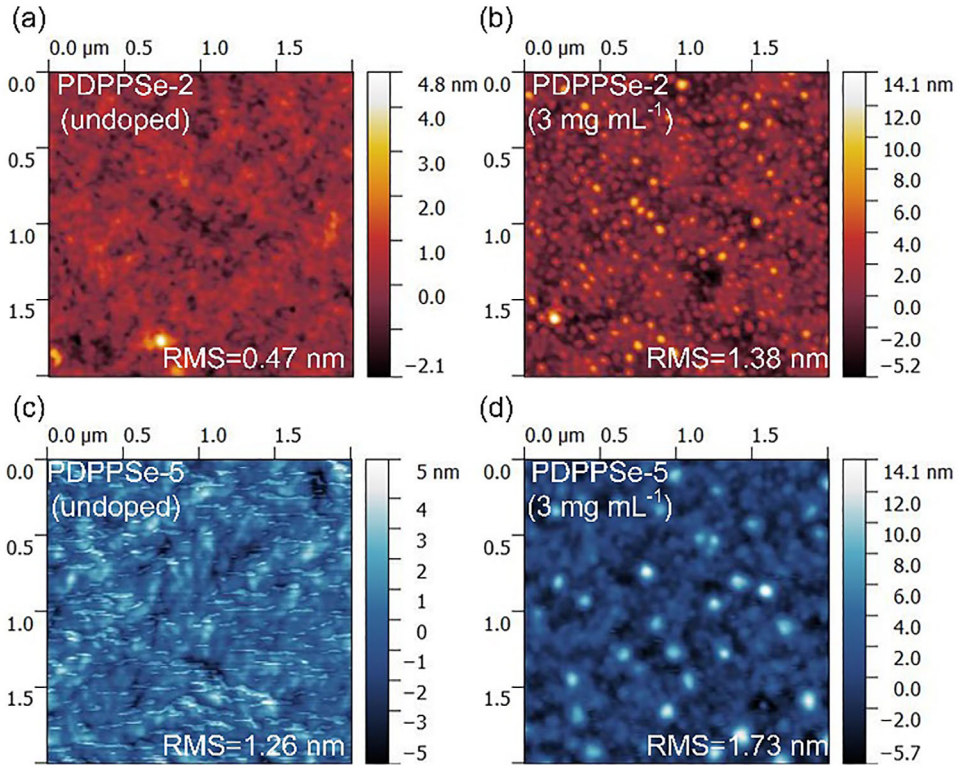

FIGURE 5 | AFM topography images of (a, b) PDPPSe-2 and (c, d) PDPPSe-5-based films (a, c) before and after doping by (c, d) 3 mg mL^{-1} $FeCl_3$.

crystalline properties of PDPPSe-5, the root mean square (RMS) roughness of the undoped PDPPSe-5 film (1.26 nm) is considerably higher than that of the pristine PDPPSe-2 films (0.47 nm) (Figure 5a,c). As the doping process proceeds, visible light spots emerge on the film surface, and as expected, the roughness of both polymer films is enhanced to varying extents by incorporating dopant molecules. Specifically, PDPPSe-2 experiences an increase to 1.38 nm, while PDPPSe-5 undergoes an increase to 1.73 nm (Figure 5b,d). This suggests that aggregation occurs upon doping, potentially impacting performance. Additionally, the data suggest that doping induces aggregation, which may influence device performance. Although the overall roughness of PDPPSe-5 remains higher, the relative increase in roughness—quantified as $\frac{RMS_{doped}-RMS_{undoped}}{RMS_{undpoed}}$, —provides a more precise measure of the doping effect. The calculated values are 1.92 for PDPPSe-2 and 0.37 for PDPPSe-5. The smaller increase in PDPPSe-5 indicates that doping perturbs its morphology less, likely because the more distant side-chain branching point provides additional free volume for dopant incorporation.

3 | Conclusions

In summary, we synthesized two D–A copolymers with identical backbones but distinct side-chain branching positions, and we elucidated how this subtle structural modification governs thermoelectric transport. PDPPSe-5, with a more distant branching point, exhibits tighter molecular packing, enhanced charge-carrier delocalization, and correspondingly higher electrical conductivity. In contrast, PDPPSe-2 exhibits greater energetic disorder and a broader density-of-states distribution, resulting in a larger Seebeck coefficient. Despite their different σ–S characteristics, both polymers deliver comparable maximum power factors, reflecting compensating contributions from conductivity and Seebeck response. These findings reveal side-chain branching as a key molecular design parameter that intrinsically modulates the coupling between σ and S, offering a new strategy for optimizing organic thermoelectric materials.

4 | Experimental Section

4.1 | Materials

The specific synthetic steps of PDPPSe-2 and PDPPSe-5 can be found in previous work [47, 48]. The molecular weight of the two polymers was measured by GPC, and the results are shown in Figure S1. Chlorobenzene (anhydrous) was purchased from Sigma–Aldrich. Anhydrous iron(III) chloride ($FeCl_3$) was purchased from Adamas-beta. Nitromethane (CH_3NO_2) was purchased from Aldrich, and acetonitrile (anhydrous) was purchased from Innochem.

4.2 | Film Fabrication and Chemical Doping

The substrates were sequentially ultrasonically cleaned in deionized water, acetone, and ethanol for 15 min each. The substrates were cleaned with plasma treatment for 15 min before use. PDPPSe-2 and PDPPSe-5 were dissolved in chlorobenzene with a concentration of 5 mg mL^{-1}. These films were prepared by blade coating and then dried at 120°C to remove the solvent, resulting in a thickness of 600 nm. Dopant solutions at different

concentrations were prepared by dissolving FeCl3 in Acetonitrile to yield solution molarities of 1, 3, 5, and 7 mg mL^{-1}. The films were then immersed in the dopant solution for 1 min. Finally, 80 nm of Au was thermally evaporated at a rate of 0.5 Å s^{-1} under a pressure of 5×10^{-5} Pa. All film preparation and doping procedures were performed in the glove box. To prevent $FeCl_3$ de-doping, conductivity measurements were performed in situ within the glove box immediately after fabrication. For external characterizations requiring sample transfer (e.g., GIWAXS), samples were stored in vacuum boxes prior to measurement.

Acknowledgements

P G acknowledges the financial support from the CAS-VPST Silk Road Science Fund: 2022. and Iran National Science Foundation (INSF) No. 4000748; "Hundred Talents Program" of the Haixi Institute, Chinese Academy of Sciences, and Fujian Province, the "Global Talent Recruitment Program" of the Government of China. We thank UNIST Office of Research Facilities and Training (ResFacT) for support of using the equipment. 2D-GIXD experiments were performed at PLS-II 3C SAXS I, 9A U-SAXS, and 6D UNIST-PAL beamlines of Pohang Accelerator Laboratory in Korea. This work was supported by the Nano & Material Technology Development Program through the National Research Foundation of Korea (NRF) funded by Ministry of Science and ICT (RS-2025-25442266) (50% contribution to this work) and the InnoCORE program of the Ministry of Science and ICT (1.260007.01).

Conflicts of Interest

The authors declare no conflicts of interest.

Data Availability Statement

The data that support the findings of this study are available in the supplementary material of this article.

References

1. O. Bubnova and X. Crispin, "Towards Polymer-Based Organic Thermoelectric Generators," *Energy & Environmental Science* 5 (2012): 9345, https://doi.org/10.1039/c2ee22777k.

2. X. Yan, M. Xiong, J.-T. Li, et al., "Pyrazine-Flanked Diketopyrrolopyrrole (DPP): a New Polymer Building Block for High-Performance n-Type Organic Thermoelectrics," *Journal of the American Chemical Society* 141 (2019): 20215–20221, https://doi.org/10.1021/jacs.9b10107.

3. O. Bubnova, Z. U. Khan, A. Malti, et al., "Optimization of the Thermoelectric Figure of Merit in the Conducting Polymer Poly(3,4-ethylenedioxythiophene)," *Nature Materials* 10 (2011): 429–433, https://doi.org/10.1038/nmat3012.

4. S. Masoumi, S. O'Shaughnessy, and A. Pakdel, "Organic-Based Flexible Thermoelectric Generators: from Materials to Devices," *Nano Energy* 92 (2022): 106774, https://doi.org/10.1016/j.nanoen.2021.106774.

5. B. Russ, A. Glaudell, J. J. Urban, M. L. Chabinyc, and R. A. Segalman, "Organic Thermoelectric Materials for Energy Harvesting and Temperature Control," *Nature Reviews Materials* 1 (2016): 16050, https://doi.org/10.1038/natrevmats.2016.50.

6. E. H. Suh, Y. J. Jeong, J. G. Oh, et al., "Doping of Donor-Acceptor Polymers with Long Side Chains via Solution Mixing for Advancing Thermoelectric Properties," *Nano Energy* 58 (2019): 585–595, https://doi.org/10.1016/j.nanoen.2019.01.075.

7. X. Zhang, H. Bronstein, A. J. Kronemeijer, et al., "Molecular Origin of High Field-Effect Mobility in an Indacenodithiophene–benzothiadiazole Copolymer," *Nature Communications* 4 (2013): 2238, https://doi.org/10.1038/ncomms3238.

8. D. Venkateshvaran, M. Nikolka, A. Sadhanala, et al., "Approaching Disorder-Free Transport in High-Mobility Conjugated Polymers," *Nature* 515 (2014): 384–388, https://doi.org/10.1038/nature13854.

9. J. Tang, Y.-H. H. Pai, and Z. Liang, "Strategic Insights into Semiconducting Polymer Thermoelectrics by Leveraging Molecular Structures and Chemical Doping," *ACS Energy Letters* 7 (2022): 4299–4324, https://doi.org/10.1021/acsenergylett.2c02119.

10. Z. Liu, Y. Hu, P. Li, J. Wen, J. He, and X. Gao, "Enhancement of the Thermoelectric Performance of DPP Based Polymers by Introducing One 3,4-ethylenedioxythiophene Electron-Rich Building Block," *Journal of Materials Chemistry C* 8 (2020): 10859–10867, https://doi.org/10.1039/D0TC01047B.

11. K. Shi, F. Zhang, C. Di, et al., "Toward High Performance n -Type Thermoelectric Materials by Rational Modification of BDPPV Backbones," *Journal of the American Chemical Society* 137 (2015): 6979–6982, https://doi.org/10.1021/jacs.5b00945.

12. A. J. Kronemeijer, V. Pecunia, D. Venkateshvaran, et al., "Two-Dimensional Carrier Distribution in Top-Gate Polymer Field-Effect Transistors: Correlation between Width of Density of Localized States and Urbach Energy," *Advanced Materials* 26 (2014): 728–733, https://doi.org/10.1002/adma.201303060.

13. A. J. Kronemeijer, E. Gili, M. Shahid, et al., "A Selenophene-Based Low-Bandgap Donor–Acceptor Polymer Leading to Fast Ambipolar Logic," *Advanced Materials* 24 (2012): 1558–1565, https://doi.org/10.1002/adma.201104522.

14. D. Huang, H. Yao, Y. Cui, et al., "Conjugated-Backbone Effect of Organic Small Molecules for n-Type Thermoelectric Materials with ZT over 0.2," *Journal of the American Chemical Society* 139 (2017): 13013–13023, https://doi.org/10.1021/jacs.7b05344.

15. L. Deng, Y. Liu, Y. Zhang, S. Wang, and P. Gao, "Organic Thermoelectric Materials: Niche Harvester of Thermal Energy," *Advanced Functional Materials* 33 (2023): 2210770, https://doi.org/10.1002/adfm.202210770.

16. S. D. Kang and G. J. Snyder, "Charge-Transport Model for Conducting Polymers," *Nature Materials* 16 (2017): 252–257, https://doi.org/10.1038/nmat4784.

17. S. A. Gregory, R. Hanus, A. Atassi, et al., "Quantifying Charge Carrier Localization in Chemically Doped Semiconducting Polymers," *Nature Materials* 20 (2021): 1414–1421, https://doi.org/10.1038/s41563-021-01008-0.

18. Y. Zhang, L. Deng, Y. Cho, et al., "Revealing the Enhanced Thermoelectric Properties of Controllably Doped Donor-Acceptor Copolymer: the Impact of Regioregularity," *Small* 19 (2023): 2206233, https://doi.org/10.1002/smll.202206233.

19. S. N. Patel, A. M. Glaudell, D. Kiefer, and M. L. Chabinyc, "Increasing the Thermoelectric Power Factor of a Semiconducting Polymer by Doping from the Vapor Phase," *ACS Macro Letters* 5 (2016): 268–272, https://doi.org/10.1021/acsmacrolett.5b00887.

20. Y. Sun, P. Sheng, C. Di, et al., "Organic Thermoelectric Materials and Devices Based on p - and n -Type Poly(metal 1,1,2,2-ethenetetrathiolate)s," *Advanced Materials* 24 (2012): 932–937, https://doi.org/10.1002/adma.201104305.

21. G. Zuo, X. Liu, M. Fahlman, and M. Kemerink, "High Seebeck Coefficient in Mixtures of Conjugated Polymers," *Advanced Functional Materials* 28 (2018): 1703280, https://doi.org/10.1002/adfm.201703280.

22. G. Zuo, Z. Li, E. Wang, and M. Kemerink, "High Seebeck Coefficient and Power Factor in n-Type Organic Thermoelectrics," *Advanced Electronic Materials* 4 (2018): 1700501, https://doi.org/10.1002/aelm.201700501.

23. D. Scheunemann, V. Vijayakumar, H. Zeng, et al., "Rubbing and Drawing: Generic Ways to Improve the Thermoelectric Power Factor of Organic Semiconductors?," *Advanced Electronic Materials* 6 (2020): 2000218, https://doi.org/10.1002/aelm.202000218.

24. Y. Zhong, G. Liu, Y. Su, et al., "Diammonium Molecular Configuration-Induced Regulation of Crystal Orientation and Carrier Dynamics for Highly Efficient and Stable 2D/3D Perovskite Solar Cells," *Angewandte Chemie International Edition* 61 (2022): 61, https://doi.org/10.1002/anie.202114588.

25. Z. Hu, D. Zhao, Y. Li, et al., "Realizing High Electrical Conductivity in Chlorine-Doped Bi_2S_3 Thermoelectric Thin Films via Air Plasma Treatment," *ACS Materials Letters* 5 (2023): 2987–2999, https://doi.org/10.1021/acsmaterialslett.3c00700.

26. N. Chen, D. Luo, P. Chen, et al., "Universal Band Alignment Rule for Perovskite/Organic Heterojunction Interfaces," *ACS Energy Letters* 8 (2023): 1313–1321, https://doi.org/10.1021/acsenergylett.2c02856.

27. R. Kroon, D. A. Mengistie, D. Kiefer, et al., "Thermoelectric Plastics: from Design to Synthesis, Processing and Structure–property Relationships," *Chemical Society Reviews* 45 (2016): 6147–6164, https://doi.org/10.1039/C6CS00149A.

28. Y. Xu, H. Sun, A. Liu, et al., "Doping: a Key Enabler for Organic Transistors," *Advanced Materials* 30 (2018): 1801830, https://doi.org/10.1002/adma.201801830.

29. J. A. Reedijk, H. C. F. Martens, H. B. Brom, and M. A. J. Michels, "Dopant-Induced Crossover from 1D to 3D Charge Transport in Conjugated Polymers," *Physical Review Letters* 83 (1999): 3904–3907, https://doi.org/10.1103/PhysRevLett.83.3904.

30. A. D. Scaccabarozzi, A. Basu, F. Aniés, et al., "Doping Approaches for Organic Semiconductors," *Chemical Reviews* 122 (2022): 4420–4492, https://doi.org/10.1021/acs.chemrev.1c00581.

31. I. E. Jacobs, Y. Lin, Y. Huang, et al., "High-Efficiency Ion-Exchange Doping of Conducting Polymers," *Advanced Materials* 34 (2022): 2102988, https://doi.org/10.1002/adma.202102988.

32. J. L. Bredas and G. B. Street, "Polarons, Bipolarons, and Solitons in Conducting Polymers," *Accounts of Chemical Research* 18 (1985): 309–315, https://doi.org/10.1021/ar00118a005.

33. S. A. Gregory, A. K. Menon, S. Ye, D. S. Seferos, J. R. Reynolds, and S. K. Yee, "Effect of Heteroatom and Doping on the Thermoelectric Properties of Poly(3-alkylchalcogenophenes)," *Advanced Energy Materials* 8 (2018): 1802419, https://doi.org/10.1002/aenm.201802419.

34. R. Ghosh and F. C. Spano, "Excitons and Polarons in Organic Materials," *Accounts of Chemical Research* 53 (2020): 2201–2211, https://doi.org/10.1021/acs.accounts.0c00349.

35. F. C. Spano, "The Spectral Signatures of Frenkel Polarons in H- and J-Aggregates," *Accounts of Chemical Research* 43 (2010): 429–439, https://doi.org/10.1021/ar900233v.

36. E. H. Suh, S. B. Kim, H. S. Yang, and J. Jang, "Regulating Competitive Doping in Solution-Mixed Conjugated Polymers for Dramatically Improving Thermoelectric Properties," *Advanced Functional Materials* 32 (2022): 2207413, https://doi.org/10.1002/adfm.202207413.

37. A. M. Glaudell, J. E. Cochran, S. N. Patel, and M. L. Chabinyc, "Impact of the Doping Method on Conductivity and Thermopower in Semiconducting Polythiophenes," *Advanced Energy Materials* 5 (2015): 1401072, https://doi.org/10.1002/aenm.201401072.

38. X. Wang, Z. Yu, Y. Lu, et al., "Density of States Engineering of n-Doped Conjugated Polymers for High Charge Transport Performances," *Advanced Materials* 35 (2023): 2300634.

39. J. Liu, G. Ye, B. van der Zee, et al., "N-Type Organic Thermoelectrics of Donor–Acceptor Copolymers: Improved Power Factor by Molecular Tailoring of the Density of States," *Advanced Materials* 30 (2018): 1804290, https://doi.org/10.1002/adma.201804290.

40. A. Abtahi, S. Johnson, S. M. Park, et al., "Designing π-Conjugated Polymer Blends with Improved Thermoelectric Power Factors," *Journal of Materials Chemistry A* 7 (2019): 19774–19785, https://doi.org/10.1039/C9TA07464C.

41. Z. Li, D. Scheunemann, D. Derewjanko, Y. Liu, M. Kemerink, and G. Zuo, "A Universal Soft Upper Limit to the Seebeck Coefficient in Organic Thermoelectrics," *Joule* 9 (2025): 102140, https://doi.org/10.1016/j.joule.2025.102140.

42. G. Garcia-Belmonte, E. V. Vakarin, J. Bisquert, and J. P. Badiali, "Doping-Induced Broadening of the Hole Density-of-States in Conducting Polymers," *Electrochimica Acta* 55 (2010): 6123–6127, https://doi.org/10.1016/j.electacta.2009.08.019.

43. M. Upadhyaya, C. J. Boyle, D. Venkataraman, and Z. Aksamija, "Effects of Disorder on Thermoelectric Properties of Semiconducting Polymers," *Scientific Reports* 9 (2019): 5820.

44. D. Mendels and N. Tessler, "Thermoelectricity in Disordered Organic Semiconductors under the Premise of the Gaussian Disorder Model and Its Variants," *The Journal of Physical Chemistry Letters* 5 (2014): 3247–3253, https://doi.org/10.1021/jz5016058.

45. J. Liu, L. Qiu, R. Alessandri, et al., "Enhancing Molecular n-Type Doping of Donor–Acceptor Copolymers by Tailoring Side Chains," *Advanced Materials* 30 (2018): 1704630, https://doi.org/10.1002/adma.201704630.

46. D. Kiefer, A. Giovannitti, H. Sun, et al., "Enhanced n-Doping Efficiency of a Naphthalenediimide-Based Copolymer through Polar Side Chains for Organic Thermoelectrics," *ACS Energy Letters* 3 (2018): 278–285, https://doi.org/10.1021/acsenergylett.7b01146.

47. J. Lee, A.-R. Han, J. Kim, Y. Kim, J. H. Oh, and C. Yang, "Solution-Processable Ambipolar Diketopyrrolopyrrole–Selenophene Polymer with Unprecedentedly High Hole and Electron Mobilities," *Journal of the American Chemical Society* 134 (2012): 20713–20721, https://doi.org/10.1021/ja308927g.

48. A.-R. Han, G. K. Dutta, J. Lee, et al., "ε -Branched Flexible Side Chain Substituted Diketopyrrolopyrrole-Containing Polymers Designed for High Hole and Electron Mobilities," *Advanced Functional Materials* 25 (2015): 247–254, https://doi.org/10.1002/adfm.201403020.

Supporting Information

Additional supporting information can be found online in the Supporting Information section.

Supporting File: aelm70348-sup-0001-SuppMat.docx.